Monthly Notices
of the
ROYAL ASTRONOMICAL SOCIETY

MNRAS **436,** 1258–1267 (2013) doi:10.1093/mnras/stt1645
Advance Access publication 2013 September 26

An early and comprehensive millimetre and centimetre wave and X-ray study of SN 2011dh: a non-equipartition blast wave expanding into a massive stellar wind

Assaf Horesh,[1⋆] Christopher Stockdale,[2,3] Derek B. Fox,[4] Dale A. Frail,[5] John Carpenter,[1] S. R. Kulkarni,[1] Eran O. Ofek,[1,6] Avishay Gal-Yam,[6] Mansi M. Kasliwal,[1,7] Iair Arcavi,[6] Robert Quimby,[8] S. Bradley Cenko,[9] Peter E. Nugent,[9,10] Joshua S. Bloom,[9,10] Nicholas M. Law,[11] Dovi Poznanski,[12] Evgeny Gorbikov,[12] David Polishook,[6,13] Ofer Yaron,[6] Stuart Ryder,[14] Kurt W. Weiler,[15] Franz Bauer,[16,17] Schuyler D. Van Dyk,[18] Stefan Immler,[19,20,21] Nino Panagia,[22,23,24] Dave Pooley[25] and Namir Kassim[26]

[1]*Cahill Center for Astrophysics, California Institute of Technology, Pasadena, CA 91125, USA*
[2]*Department of Physics, Marquette University, PO Box 1881, Milwaukee, WI 53201, USA*
[3]*Homer L. Dodge Department of Physics & Astronomy, The University of Oklahoma, Norman, OK 73019, USA*
[4]*Astronomy and Astrophysics, Eberly College of Science, The Pennsylvania State University, University Park, PA 16802, USA*
[5]*National Radio Astronomy Observatory, PO Box 0, Socorro, NM 87801, USA*
[6]*Benoziyo Center for Astrophysics, Faculty of Physics, The Weizmann Institute of Science, Rehovot 76100, Israel*
[7]*Carnegie Institution for Science, 813 Santa Barbara St, Pasadena, CA 91101, USA*
[8]*IPMU, University of Tokyo, Kashiwanoha 5-1-5, Kashiwa-shi, Chiba, Japan*
[9]*Department of Astronomy, University of California, Berkeley, CA 94720-3411, USA*
[10]*Computational Cosmology Center, Lawrence Berkeley National Laboratory, 1 Cyclotron Road, Berkeley, CA 94720, USA*
[11]*Dunlap Institute for Astronomy and Astrophysics, University of Toronto, 50 St. George Street, Toronto M5S 3H4, Ontario, Canada*
[12]*School of Physics and Astronomy, Tel-Aviv University, Tel-Aviv 69978, Israel*
[13]*Department of Earth, Atmospheric, and Planetary Sciences, Massachusetts Institute of Technology, Cambridge, MA 02139, USA*
[14]*Australian Astronomical Observatory, PO Box 915, North Ryde, NSW 1670, Australia*
[15]*Computational Physics Inc., 8001 Braddock Road, Suite 210, Springfield, VA 22151-2110, USA*
[16]*Instituto de Astrofísica, Facultad de Física, Pontificia Universidad Catlica de Chile, 306, Santiago 22, Chile*
[17]*Space Science Institute, 4750 Walnut Street, Suite 205, Boulder, CO 80301, USA*
[18]*Spitzer Science Center/Caltech, Mailcode 220-6, Pasadena, CA 91125, USA*
[19]*Astrophysics Science Division, NASA Goddard Space Flight Center, Greenbelt, MD 20771, USA*
[20]*Department of Astronomy, University of Maryland, College Park, MD 20742, USA*
[21]*Center for Research and Exploration in Space Science and Technology, NASA Goddard Space Flight Center, Greenbelt, MD 20771, USA*
[22]*Space Telescope Science Institute, 3700 San Martin Drive, Baltimore, MD 21218, USA*
[23]*INAFCT, Osservatorio Astrofisico di Catania, Via S. Sofia 78, I-95123 Catania, Italy*
[24]*Supernova Limited, OYV #131, Northsound Road, Virgin Gorda, British Virgin Islands*
[25]*Department of Astronomy, University of Texas, Austin, TX 78712, USA*
[26]*Naval Research Laboratory, Code 7213, Washington, DC 20375-5320, USA*

Accepted 2013 August 30. Received 2013 August 30; in original form 2013 June 5

ABSTRACT

Only a handful of supernovae (SNe) have been studied in multiwavelengths from the radio to X-rays, starting a few days after the explosion. The early detection and classification of the nearby Type IIb SN 2011dh/PTF 11eon in M51 provides a unique opportunity to conduct such observations. We present detailed data obtained at one of the youngest phase ever of a core-collapse SN (days 3–12 after the explosion) in the radio, millimetre and X-rays; when combined with optical data, this allows us to explore the early evolution of the SN blast wave

⋆E-mail: assafh@astro.caltech.edu

and its surroundings. Our analysis shows that the expanding SN shock wave does not exhibit equipartition ($\epsilon_e/\epsilon_B \sim 1000$), and is expanding into circumstellar material that is consistent with a density profile falling like R^{-2}. Within modelling uncertainties we find an average velocity of the fast parts of the ejecta of $15\,000 \pm 1800\,\mathrm{km\,s^{-1}}$, contrary to previous analysis. This velocity places SN 2011dh in an intermediate blast wave regime between the previously defined compact and extended SN Type IIb subtypes. Our results highlight the importance of early ($\sim$1 d) high-frequency observations of future events. Moreover, we show the importance of combined radio/X-ray observations for determining the microphysics ratio ϵ_e/ϵ_B.

Key words: supernovae: general – supernovae: individual: SN 2011dh – radio continuum: general – X-rays: general.

1 INTRODUCTION

SN 2011dh in the nearby galaxy Messier 51 (M51) was discovered on UTC 2011 May 31.893 by A. Riou, detected on UTC June 01.19 by the Palomar Transient Factory (PTF, Law et al. 2009; Rau et al. 2009) and rapidly spectroscopically classified as a Type IIb supernova (SN; Arcavi et al. 2011a,b).

The proximity of M51 (as in Arcavi et al. 2011a we assume a distance $d = 8.03 \pm 0.77$ Mpc) motivated searches for the progenitor star. A putative massive star detected by the *Hubble Space Telescope* in pre-explosion images of M51 very close to the SN position was described by Maund et al. (2011) and Van Dyk et al. (2011). The interpretation of the progenitor is uncertain. Based on the rapid cooling of the expanding SN ejecta, Arcavi et al. (2011a) argue that the progenitor star must have a radius smaller than that of typical red supergiants or the supergiant progenitor of the well-studied Type IIb SN 1993J (see e.g. Weiler et al. 2007) ($R < 10^{13}$ cm). In contrast, the astrometrically coincident star is a F8 supergiant. One way of reconciling these constraints means that the supergiant is either unrelated to the SN or was a companion of the (now erstwhile) progenitor star. However, recently, Bersten et al. (2012) and Benvenuto, Bersten & Nomoto (2013) performed hydrodynamical simulations, showing that the early light curve of SN 2011dh is consistent with a yellow supergiant progenitor.

For core-collapse SNe, the interaction of the blast wave with the circumstellar medium can generate detectable radio and X-ray emission. Additionally, the fastest moving ejecta are related to the size of the progenitor (the more compact, the higher the velocity; Chevalier & Soderberg 2010). These two properties motivate early radio and X-ray observations. Thus, we began a programme of centimetre and millimetre wave observations of SN 2011dh with the Expanded Very Large Array (EVLA; Perley et al. 2011) and the Combined Array for Research in Millimeter-wave Astronomy (CARMA), respectively. We initiated X-ray observations with the *Swift* observatory. Following the end of our early monitoring, a long-term programme at the EVLA was launched by A. Soderberg and collaborators. Their results are reported in a recent paper by Krauss et al. (2012).

Soderberg et al. (2012) analysed the *Swift* X-ray and two epochs (day 4 and day 17) of radio observations of SN 2011dh, and found an expansion speed of $\approx 0.1c$ and a mass-loss rate of $6 \times 10^{-5}\,\mathrm{M_\odot\,yr^{-1}}$. With these inferences they concluded that SN 2011dh is probably a Type cIIb SN, namely an SN that originated from a compact progenitor star as opposed to one that originated from an extended progenitor star (Type eIIb) (see Chevalier & Soderberg 2010, and references therein for an explanation of these proposed subtypes). A similar result was found by Krauss et al. (2012).

Here we present a full set of centimetre and millimetre wave observations (from day 3 to day 12 after the explosion) as well as an analysis of the *Swift* and *Chandra* X-ray observations of SN 2011dh. To our knowledge, these represent the most comprehensive (essentially daily) set of pan radio (5–100 GHz) observations obtained at early times of a core-collapse SN. As a result we are able to probe the circumstellar matter (CSM) at smaller radii (wherein one can expect to find deviations from homologous flows) and in principle directly infer the density of CSM.

The paper is organized as follows. The millimetre (CARMA) and centimetre (EVLA) observations are summarized in Section 2 and the X-ray observations are summarized in Section 3. In Section 4, we carry out a standard analysis for the radio observations assuming a synchrotron self-absorbed model. We then present a combined radio+X-ray analysis (which incorporates inverse Compton scattering of optical photons to the X-ray band) in Section 5. We present our conclusions as well as review the returns obtained from early millimetre wave observations of core-collapse SNe (Section 6). Such a review is timely, given the imminent operation of the Atacama Large Millimeter Array (ALMA).

2 CARMA AND EVLA OBSERVATIONS

Starting 2011 June 4, observations were undertaken with the CARMA, centred on either 107 or 93 GHz with an 8 GHz bandwidth in the D array configuration. For flux calibration we used either Uranus (whose flux was bootstrapped from observations of 3C 345) or Mars. The compact source J1153+495 was used as a phase calibrator. The CARMA data were reduced using the MIRIAD reduction software.[1] The log of observations can be found in Table 1 and a montage of CARMA detections is shown in Fig. 1.

Observations with the EVLA were undertaken in the framework of our programme 'PTF Transients in the Local Universe' (PI: Kasliwal) as well as a ToO program to observe Type II SNe (PI: C. Stockdale). The array configuration was A. 3C 286 served as the flux calibrator. We used the AIPS software to reduce the EVLA data. The first EVLA detection of the SN was in both the *K* (22.46 GHz) and the *Q* (43.46 GHz) bands at fluxes of 2.6 and 6.95 mJy, respectively. The log of the observations can be found in Table 1.

3 X-RAY OBSERVATIONS

SN 2011dh was observed with the *Swift* X-ray telescope (XRT; Burrows et al. 2003) in a series of observations beginning on 2011 June 3.5. We analysed all observations taken through 2011 June 23

[1] http://bima.astro.umd.edu/miriad/

Table 1. Summary of early radio observations of SN 2011dh.

Day	Frequency (GHz)	Flux (mJy)
4.21	4.8	$\leq$0.17
4.21	7.4	$0.203 \pm 0.036 \pm 0.01$
4.25	22.5	$2.6 \pm 0.07 \pm 0.26$
4.23	43.2	$6.95 \pm 0.17 \pm 0.7$
4.08	107	$4.55 \pm 0.33 \pm 0.46$
4.08	230	$\leq$3
5.01	8.5	$0.455 \pm 0.046 \pm 0.023$
5.12	22.5	$3.95 \pm 0.07 \pm 0.4$
5.10	43.2	$6.47 \pm 0.14 \pm 0.65$
5.22	107	$3.66 \pm 0.35 \pm 0.36$
6.92	93	$2.52 \pm 0.27 \pm 0.25$
7.12	8.5	$1.06 \pm 0.03 \pm 0.053$
7.20	43.2	$6.42 \pm 0.17 \pm 0.64$
7.22	22.5	$6.89 \pm 0.06 \pm 0.69$
8.91	93	$1.84 \pm 0.31 \pm 0.18$
9.02	22.5	$7.46 \pm 0.04 \pm 0.75$
9.02	8.5	$1.58 \pm 0.03 \pm 0.079$
9.06	5.0	$0.42 \pm 0.03 \pm 0.021$
9.12	33.6	$7.49 \pm 0.06 \pm 0.75$
10.95	93	$1.61 \pm 0.30 \pm 0.16$
11.01	43.2	$3.19 \pm 0.15 \pm 0.32$
11.03	22.5	$8.17 \pm 0.05 \pm 0.82$
11.98	8.5	$3.15 \pm 0.06 \pm 0.158$
12.02	5.0	$1.22 \pm 0.03 \pm 0.061$
12.91	93	$1.06 \pm 0.31 \pm 0.106$
15.08	93	$1.05 \pm 0.17 \pm 0.105$

Notes. Day is given in UT days in 2011 June. The errors presented in the table represent the rms error from each image and a systematic calibration error (5 per cent for $\nu < 20$ GHz and 10 per cent for $\nu > 20$ GHz) that should be combined in quadrature.

using the pipeline software of the UK Swift Science Data Centre at the University of Leicester[2] (hereafter UK SSDC; Evans et al. 2007). To generate the X-ray light curve (see Fig. 2), we fix the source position at the known location of the SN and extract a light curve with half-day binning (43.2 ks per time bin) using an aperture of 35.4 arcsec. For background subtraction, we determine the time-average count rate in this identical aperture, 1.29 ± 0.14 counts ks^{-1} (0.3–10 keV), from pre-SN 2011dh *Swift* data.

The SN X-ray emission appears to fade rapidly at early times, so we split the observations in two for purposes of X-ray spectral analysis, fitting data from the first three time bins separately from the rest. The data are then fitted to X-ray spectral models in XSPEC v 12.7.0 (Arnaud 1996), using a common hydrogen column density ($N_{\rm H}$) across the full duration of the *Swift* observations and allowing the power-law photon (Γ) index and time-average flux to vary between the two data sets. The resulting fit yields the following spectral parameters, where uncertainties here and below are quoted at 90 per cent confidence: $N_{\rm H} = 1.1^{+1.3}_{-1.1} \times 10^{21}$ cm^{-2}; $\Gamma_1 = 1.1 \pm 0.4$; and $\Gamma_2 = 1.9^{+0.3}_{-0.4}$. The results suggest a softening of the X-ray emission over the course of the *Swift* observations, but note that the photon index overlaps for $\Gamma = 1.5$ at the 90 per cent confidence intervals.

Prior to analysing the resulting X-ray flux light curve (Fig. 2), we incorporate *Chandra* X-ray flux measurements from Pooley (2011) and Soderberg et al. (2012); these are converted to our chosen 0.3–10 keV bandpass using the authors' chosen spectral models and the WEBPIMMS tool.[3] The *Swift* and *Chandra* measurements are summarized in Table 2. Analysing the resulting X-ray light curve, we find that it may be adequately characterized (in a χ^2 sense) as a monotonic power-law decay emission. The single power-law temporal decay index is $s_{\rm X} = -1.2 \pm 0.2$ over the interval of *Swift* and *Chandra* observations. The *Chandra* data confirm the absence of significant contaminating source emission within the *Swift* XRT aperture (Pooley 2011; Soderberg et al. 2012).

4 STANDARD SYNCHROTRON ANALYSIS

In this section, we perform an analysis based on the radio data alone. Throughout this section, we assume equipartition (see details below). A combined radio–X-ray–optical analysis is presented in the next section (Section 5).

The radio emission arises from relativistic particles, which are accelerated at the shock, gyrating in magnetic fields generated in the post-shock gas (Chevalier 1982, 1998; Weiler et al. 2002). A large body of work confirms that (for most SNe) the early radio emission can be described by a synchrotron self-absorption (SSA) model (Chevalier 1998; Chevalier & Fransson 2006; Chevalier & Soderberg 2010). While internal free–free absorption might also be present at early times, the lack of a steeper spectrum at the optically-thick part of the spectrum suggests that SSA is dominant (see also Appendix A). Hence, throughout this paper, we adopt the Chevalier (1998) SSA model.

Assuming a power law for the energy of the relativistic particles, the synchrotron emission for a self-absorbed source can be described by

$$S_\nu \propto \frac{\pi R^2}{D^2} B^{-1/2} \nu^{5/2} \text{ (optically thick)} \quad (1)$$

for frequency ν below $\nu_{\rm a}$, where $\nu_{\rm a}$ is the frequency at which the optical depth from synchrotron self-absorption is unity, and

$$S_\nu \propto \frac{4\pi f R^3}{3D^2} N_0 B^{(p+1)/2} \nu^{-(p-1)/2} \text{ (optically thin)} \quad (2)$$

for frequencies above $\nu_{\rm a}$. Here B is the the strength of the magnetic field, R is the radius of the blast wave, D is the distance from the observer to the SN, f is the volume fraction of the radio-emitting region and the energy spectrum of the relativistic particles is given by a power law $N(E) = N_0 E^{-p}$.

The SSA model does not attempt to predict the absolute or even the relative fraction of the two key components: the energy in relativistic electrons and the strength of the magnetic field. However, the minimum total energy will be achieved at equipartition, i.e. when the energy in the relativistic electrons is equal to that of the magnetic fields or $f_{eB} = 1$ (see Readhead 1994). Here $f_{eB} = 1$ is the ratio of the fraction of shock wave energy in relativistic electrons ($\epsilon_{\rm e}$) to that of the fraction of shock wave energy converted to the magnetic fields (ϵ_B).

The measurement of the single-epoch SSA spectrum (both the optically-thick and the optically-thin parts) can be inverted to yield the radius and the magnetic field at that epoch (Chevalier 1998).

[2] UK Swift Science Data Centre: http://www.swift.ac.uk/

[3] WEBPIMMS tool: http://heasarc.gsfc.nasa.gov/Tools/w3pimms.html

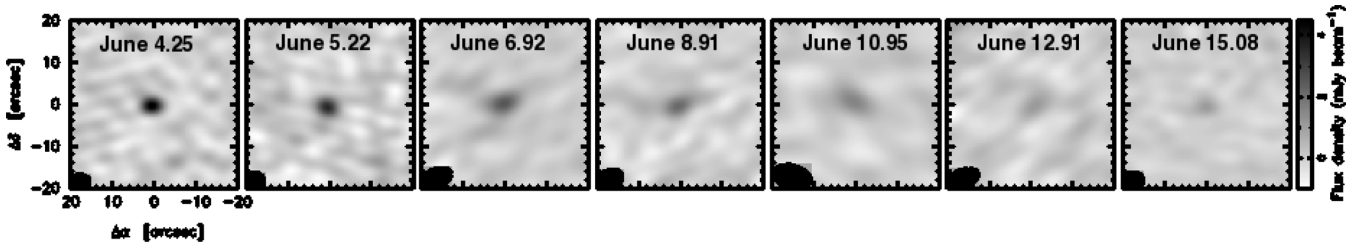

Figure 1. CARMA image cutouts of SN 2011dh in the 3-mm band. The source at the centre is SN 2011dh. The image cutouts are 40 arcsec on a side centred around SN 2011dh's most precise position, based on our EVLA observations, at RA = 13:30:05.104 and Dec. = 47:10:10.915 (J2000.0). The positional error is ±0.01 arcsec on each axis (see text).

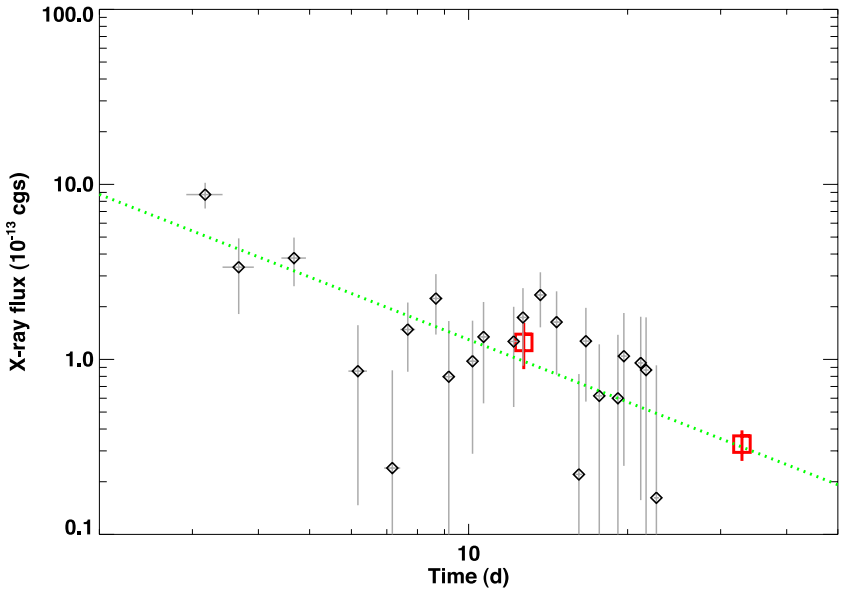

Figure 2. X-ray light curve of SN 2011dh (0.3–10 keV) as determined from *Swift* XRT observations (black diamonds) and the high-level analysis software at the UK SSDC (Evans et al. 2007). Error bars are 1σ. Data have been binned to half-day intervals, with bins having less than 5 per cent coverage dropped from analysis, and converted from counts to flux using the results of our X-ray spectral fits. The two red squares are *Chandra* measurements converted to the (0.3–10 keV) band. A fit to the temporal decay is indicated as a single-power-law decay (dotted green line). Counts-to-flux conversion factors (*Swift* observations) for the two spectral epochs (the first three bins and the rest of the bins) are $c_{1,a} = 8.3 \times 10^{-11}$ and $c_{2,a} = 5.3 \times 10^{-11}$ erg cm^{-2} s^{-1} counts^{-1}, respectively, with respect to 0.3–10 keV absorbed flux, and $c_1 = 8.8 \times 10^{-11}$ and $c_2 = 6.7 \times 10^{-11}$ erg cm^{-2} s^{-1} counts^{-1}, respectively, for 0.3–10 keV unabsorbed flux. The latter are the counts-to-flux conversion factors we use to generate the X-ray flux light curve for SN 2011dh.

For $p = 3$ (which is the relevant case here; see Section 4.1)

$$R_{\rm p} = 8.8 \times 10^{15} f_{eB}^{-1/19} \left(\frac{f}{0.5}\right)^{-1/19} \left(\frac{S_{\rm p}}{\rm Jy}\right)^{9/19} \left(\frac{D}{\rm Mpc}\right)^{18/19} \times \left(\frac{\nu_{\rm p}}{5\,\rm GHz}\right)^{-1} \rm cm \quad (3)$$

and

$$B_{\rm p} = 0.58 f_{eB}^{-4/19} \left(\frac{f}{0.5}\right)^{-4/19} \left(\frac{S_{\rm p}}{\rm Jy}\right)^{-2/19} \left(\frac{D}{\rm Mpc}\right)^{-4/19} \times \left(\frac{\nu_{\rm p}}{5\,\rm GHz}\right) \rm G. \quad (4)$$

Here, $S_{\rm p}$ is the peak flux,[4] $\nu_{\rm p}$ is the peak frequency and again f is the volume fraction of the radio-emitting region. We assume $f = 0.5$ (see Chevalier & Fransson 2006). For the general case (accounting for different values of p), see equations (11) and (12) in Chevalier (1998).

Equations (1) and (2) are adequate to describe the broad-band spectrum at any given epoch, as long as the emission is SSA. The dynamics of the SN shell (which in turn depend on the velocity profile of the blast wave and the radial density distribution of the circumstellar medium) determine R and $\nu_{\rm a}$. These dependencies are generalized by allowing for power-law variations in key quantities (Weiler et al. 2002), leading to the following equations:

$$S = K1 \left(\frac{\nu}{5\,\rm GHz}\right)^{\alpha} \left(\frac{t - t_0}{1\,\rm d}\right)^{\beta} \left(\frac{1 - {\rm e}^{-\tau_{\rm SSA}}}{\tau_{\rm SSA}}\right), \quad (5)$$

where the absorption expression describes an internal absorption by material mixed with the emitting component and assumes planar geometry. The SSA optical depth is described by

$$\tau_{\rm SSA} = K5 \left(\frac{\nu}{5\,\rm GHz}\right)^{\alpha-2.5} \left(\frac{t - t_0}{1\,\rm d}\right)^{\delta''}, \quad (6)$$

where both $K1$ and $K5$ are proportionality constants that can be determined by fitting the data, and δ'' describes the time dependence of the optical depth.

[4] The peak flux marks the transition of the spectrum from optically thick to optically thin.

Table 2. SN 2011dh X-ray flux measurements.

Mission	Time	Flux	Unc.
Swift	3.171	8.746	1.468
Swift	3.671	3.365	1.550
Swift	4.671	3.793	1.174
Swift	6.171	0.857	0.711
Swift	7.171	0.239	0.627
Swift	7.671	1.481	0.631
Swift	8.671	2.228	0.843
Swift	9.171	0.797	0.859
Swift	10.171	0.976	0.688
Swift	10.671	1.345	0.784
Swift	12.171	1.266	0.732
Swift	12.671	1.736	0.816
Chandra	12.716	1.250	0.370
Swift	13.671	2.335	0.811
Swift	14.671	1.634	0.815
Swift	16.171	0.220	0.604
Swift	16.671	1.272	0.698
Swift	17.671	0.619	0.600
Swift	19.171	0.600	0.782
Swift	19.671	1.044	0.798
Swift	21.171	0.955	0.798
Swift	21.671	0.869	0.869
Swift	22.671	0.162	0.763
Chandra	32.916	0.328	0.065

Notes. Time is measured in days from the estimated SN explosion date of May 31.58 2011 (UT). X-ray fluxes are quoted in units of 10^{-13} erg cm^{-2} s^{-1} (0.3–10 keV, unabsorbed); flux uncertainties are quoted at 1σ. *Chandra* fluxes have been converted from the published values (Pooley 2011; Soderberg et al. 2012) to our chosen energy range using WEBPIMMS (see text for details).

4.1 Blast wave physical parameters at single epochs

We analyse observations from the first five epochs: 2011 June 4, 5, 7, 9 and 11. During the first four epochs, data were obtained within a span of ≈4 h and thus are considered to be nearly simultaneous such that we assigned a central average time to all flux densities of a given epoch. We note that the last *C*- and *X*-band observations were made on June 12 rather than on June 11 and therefore we obtain the *C*- and *X*-band fluxes for June 11 by interpolation. For each epoch we fit the EVLA–CARMA spectrum[5] to the SSA model characterized by p, $S_{\rm p}$ and $\nu_{\rm p}$ (equations 1 and 2). We assume equipartition ($f_{eB} = 1$). For each epoch, the SSA model is well fitted by the data (with χ^2 values of 0.8–4.1). The fitted parameters are the absorption normalization, the synchrotron emission normalization and the electron energy power-law index, p. The electron energy index, p, averaged over the five epochs we analyse is $p = 3.0 \pm 0.4$ (where the five fitted values of p are 2.6, 2.5, 3.0, 3.4 and 3.4). Next, substituting our fitted parameters into equations (3) and (4), we derive the magnetic field (B) and radius (R) at each of our five epochs.

As shown in Fig. 3, the blast wave radius, $R \propto t^m$, where $m = 1.14 \pm 0.24$, while the magnetic field is proportional to $t^{-1 \pm 0.12}$. Theoretically, the value of m depends on the density structure of the ejecta. In particular, once the blast wave decelerates, $m = (n-3)/(n-2)$, where n is the density distribution index of the SN ejecta ($\rho_{\rm ej} \propto r^{-n}$), and assuming that the CSM density is $\rho_{\rm CSM} \propto r^{-2}$. For red supergiants (convective stars), $n = 12$, leading to $m = 0.9$, while for Wolf–Rayet (radiative) stars, $n = 7$, leading to $m = 0.8$. Unfortunately, our data lack the precision to discriminate between these two possibilities. Since theoretically[6] $m \leq 1$, we conclude that the mean velocity of the shock (computed as R/t, where t is the time since the explosion) is about 21 000 km s^{-1}. However, if the shock wave is indeed decelerating ($m < 1$), then the above shock wave velocity will be reduced by a factor of m.

Next we can place a lower limit on the total internal energy of the emitting material. In principle, in addition to the energy in the electrons and in the magnetic field, some energy can be carried by protons. We cannot estimate the proton energy. Thus, the lowest estimate of the energy is given by the equipartition analysis and excluding that carried by protons (ions):

$$E_{\rm min} = \frac{B_{\rm p}^2 R_{\rm p}^3}{6}\,(1 + f_{eB})\, f \text{ (Soderberg et al. 2010).} \quad (7)$$

This yields (assuming $f_{eB} = 1$ and $f = 0.5$) $E_{\rm min} \approx [1.6, 1.8, 2.9, 3.8, 5.8] \times 10^{45}$ erg at epochs of June 4, 5, 7, 9 and 11, respectively.

4.2 Time-dependent solution

We now fit the data to a comprehensive multi-epoch SSA model (as described by equations 5 and 6; see Fig. 4). The resulting fit parameters are $\alpha = -1.15$, $\beta = -0.96$, $K1 = 453.43$, $K5 = 1.9772 \times 10^5$ and $\delta'' = -3.42$ (with 1σ errors of 6, 8, 8, 12 and 3 per cent, respectively, and a reduced χ^2 of 2.8). This implies an electron power-law distribution with $p = 3.3$ and $R \propto t^{1.06}$ which is consistent with what we found in the single-epoch analysis we performed above. Moreover, adding an additional free–free absorption term to our fit results in a free–free absorption coefficient which is smaller by a few orders of magnitude than the SSA absorption coefficient, thus showing that that SSA is the dominant absorption mechanism.

Assuming the CSM was formed by a constant wind mass-loss,[7] the CSM density structure will have the form $\rho_{\rm CSM} \propto r^{-2}$. We next calculate the electron number density which is given by $n_{\rm e} = f_{eB} \frac{(p-2)}{(p-1)} \frac{B^2}{8\pi \gamma_{\rm m} m_{\rm e} c^2}$, where $\gamma_{\rm m}$ is the minimum electron Lorentz factor[8] (Soderberg et al. 2006). The resulting electron density is $n_{\rm e} \approx (1.6\text{–}2.5) \times 10^5 \left(\frac{R}{10^{15}\,{\rm cm}}\right)^{-2}$ cm^{-3}. In order to estimate the mass-loss rate of the progenitor via the wind prior to the explosion, $\dot{M} = 4\pi R^2 n_{\rm e} m_{\rm p} v_{\rm w}$, an assumption about the wind velocity, $v_{\rm w}$, has to be made. Following Chevalier & Fransson (2006), instead of assuming a wind velocity, we will scale the mass-loss rate by it and define a new parameter, $A = \dot{M}/4\pi v_{\rm w}$. In the case of SN 2011dh, $A \approx 5 \times 10^{11}$ g cm^{-1}, which is a factor of 3 smaller than the value derived by Soderberg et al. (2012) and Krauss et al. (2012) (under the equipartition assumption). This value of A corresponds to a mass-loss rate of $10^{-7} \times (v_{\rm w}/10\,{\rm km\,s^{-1}})$ M$_\odot$ yr^{-1}, consistent with a broad range of massive progenitor stars, from red supergiants to compact Wolf–Rayet stars.

[5] Note that we do not use the null detections in the fit.

[6] Note that measurement errors can drive the value of m above the expected theoretical value of $m \leq 1$.

[7] We assume that the CSM is ionized. This is probably not an issue for blue supergiants or Wolf–Rayet progenitors. For red supergiants, the strong ultraviolet (UV) flash essentially ionizes the CSM around the progenitor star up to at least a few times 10^{15} cm (Lundqvist & Fransson 1988; Fransson, Lundqvist & Chevalier 1996).

[8] Here we adopt a minimum Lorentz factor of $\gamma_{\rm m} = 1$ as in Chevalier (1998).

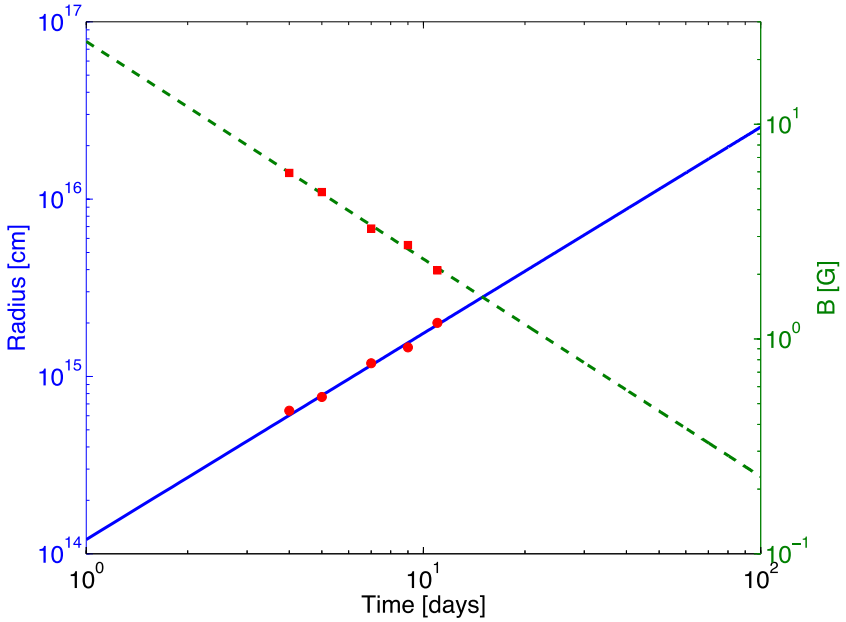

Figure 3. The blast wave radius (red circles) and magnetic field (red squares) estimates at five epochs. We assume an explosion date of 2011 May 31.5. Relative to this explosion date the epochs are [3.7, 4.6, 6.6, 8.5, 10.5] d. The corresponding values are: $R \approx [0.64, 0.77, 1.19, 1.46, 2.01] \times 10^{15}$ cm and $B \approx [5.9, 4.8, 3.3, 2.7, 2.1]$ G. Given the uncertainty in the peak fluxes, peak frequencies and p, we estimate the radius and magnetic field uncertainties to be 11 and 9 per cent, respectively. Including also an uncertainty of 10 per cent in the SN distance increases the uncertainty of the radius to 15 per cent. The curves are power-law fits with $R \propto t^{1.14 \pm 0.24}$ (solid blue line) and $B \propto t^{-1 \pm 0.12}$ (dashed green line).

5 COMBINED RADIO–X-RAY–OPTICAL ANALYSIS

The X-ray photon index is 1.1 (early times) and 1.9 (late times). The high-frequency radio spectral index is -1 which corresponds to a photon index of 2. The X-ray emission is elevated by a factor of 50 relative to extrapolation of the SSA spectrum. Thus, we conclude that the X-ray emission is not a result of synchrotron emission. Moreover, as already shown by Soderberg et al. (2012), thermal free–free X-ray emission is ruled out. Another explanation for the X-ray emission is that it arises from inverse Compton (IC) scattering of optical photons.[9]

Assuming that the X-ray emission arises from IC, the SSA and IC formulation of Katz (2012) can be used to explicitly infer B. For $p = 3$

$$B = 0.48 \left(\frac{r_{\rm SIC} F_{\rm t}}{10^{-12}\,{\rm erg\,cm^{-2}\,s^{-1}}} \right)^{2/5} \left(\frac{S_{\nu,{\rm abs}}}{\rm mJy} \right)^{-2/5} \left(\frac{\nu}{10\,{\rm GHz}} \right) {\rm G}, \quad (8)$$

where $r_{\rm SIC} = \nu S_{\nu,{\rm syn}}/(\nu S_{\nu,{\rm IC}})$, $S_{\nu,{\rm IC}}$ is the IC flux, $S_{\nu,{\rm syn}}$ is the synchrotron flux, $S_{\nu,{\rm abs}}$ is the SSA flux and $F_{\rm t}$ is the optical flux.

Applying the Katz (2012) equations to the optical (where the flux is $F_{\rm t} = (1.3\text{–}2.7) \times 10^{-10}\,{\rm erg\,cm^{-2}\,s^{-1}}$; Arcavi et al. 2011a), X-ray and radio measurements on June 7, 9 and 11 yields $B \approx [0.77, 0.68, 0.48]$ G, respectively. The estimated error (obtained from application of the rule of error propagations) is ≈15 per cent. These values of B are ≈4.2 smaller than the corresponding estimates obtained from an equipartition analysis (Section 4.1). Nominally, by using equation (4) again, $f_{eB} \approx 500\text{–}1700$ with 10^3 as a reasonable mean (which we adopt). However, as can be seen from equation (3) this only results in a 30 per cent decrease in the value of R, relative to that obtained from equipartition analysis (Section 4.1). Thus, the mean velocity is $R/t \approx 1.5 \times 10^9$ cm s^{-1}. The electron density is now higher by a factor of ∼50 and therefore the mass-loss rate is higher by a factor of ∼20 (for a fixed wind velocity).[10]

6 CONCLUSIONS AND RAMIFICATIONS

In this paper, we present the earliest millimetre and centimetre wave monitoring observations of the Type IIb SN 2011dh in the galaxy M51, between 4 d and 12 d after the event. Using the wide frequency coverage of the EVLA (4–43 GHz) and CARMA (100 GHz), we measure the key parameters of the synchrotron self-absorbed spectrum. The radio observations were accompanied by extensive X-ray observations by *Swift*. The X-ray emission, argued to be IC scattering of the SN optical photons by the relativistic electrons that produced the radio emission, combined with the radio observations, allows us to relax the equipartition assumption and track the radius and circumstellar density.

The radio data alone, under the equipartition assumption, imply an average shock wave velocity of ≈21 000 km s^{-1}. However, a combined radio–X-ray–optical analysis shows that there is a large deviation from equipartition. Based on the latter, we infer a mean velocity of $R/t \approx 1.5 \times 10^9$ cm s^{-1}, for the SN shock wave, with an uncertainty entirely dominated by the limitations of the theoretical

[9] The SSA model yields B of a few G. A $\nu_{\rm p}$ of 30 GHz would require a Lorentz factor $\gamma \sim 33$. These electrons can inverse-scatter SN optical photons to the X-ray band.

[10] In the appendix, we use the new values we find here to calculate the free–free absorption. We find that at the time of the observations, it is still negligible in the observed frequencies.

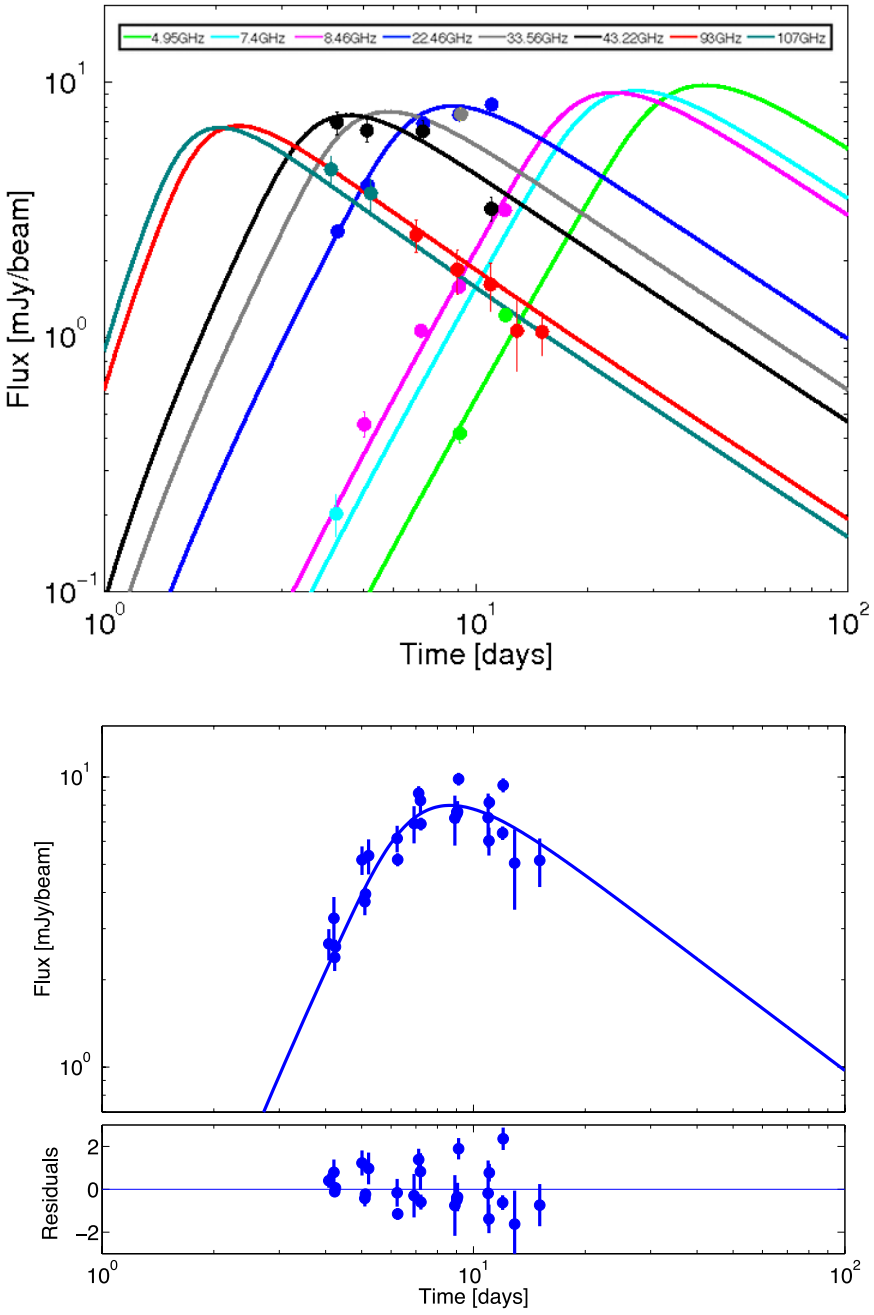

Figure 4. Radio emission as a function of time. In the upper panel, the result of the time-dependent fit (solid curves) is presented separately for each of the following frequencies: ν = [107, 93, 43.22, 33.56, 22.46, 8.46, 7.4, 4.95] GHz from the left-hand to right-hand side, respectively. In the lower panel, the time-dependent fit and its residuals for a frequency of $\nu = 22.46$ GHz are shown. The measurements presented in the lower panel were shifted to the latter frequency, assuming the fit parameters from Section 4.2.

framework. Within the framework of the model, the velocity is 1.32–1.68 $\times$ 10^9 cm s^{-1}. This value range is larger than the $\sim 10^9$ cm s^{-1} expected for an extended progenitor (red supergiant) but smaller than the $\sim 3 \times 10^9$ cm s^{-1} expected for a compact progenitor. This may have important implications for the evolution leading to the formation of the progenitors of Type IIb SNe: if Type IIb SNe are split into two distinct, well-separated classes, that would suggest they may arise from two different evolutionary scenarios. On the other hand, if additional intermediate objects are found, which may suggest a continuum of objects between Type eIIb and Type cIIb, a single progenitor class may be favoured.

We use the SSA model analysis to infer the evolution of radius with time, $R \propto t^m$. We find $m = 1.14 \pm 0.24$. The error bars are too large to directly constrain the physical nature of the envelope of the exploding star (radiative versus convective). Assuming no additional systematics, the combination of the early measurements with observations over several months may provide the means to determine the deceleration phase of the shock wave in a more precise way and indirectly may shed more light on the density profile of the outer layers of the progenitor.

Soderberg et al. (2012) infer a much higher shock wave velocity, 3×10^9 cm s^{-1}, when assuming equipartition. Fitting Soderberg

et al. (2012) radio measurements on June 17, we find that the shock wave velocity is $\approx$19 550 km s^{-1}. Moreover, as mentioned above, there is a factor of 3 difference between the derived equipartition mass-loss rate value in our analysis (Section 4.2) compared to Soderberg et al. (2012). The origin of this difference is in the way this value is calculated and in the assumptions made. While Soderberg et al. (2012) assume $\epsilon_e = 0.1$, we do not make such an assumption. Our measurements suggest $\epsilon_e \sim 0.3$ (based on Chevalier & Fransson 2006, equation 8) which accounts for the different mass-loss rate values.

As noted in Section 1, the Soderberg et al. (2012) analysis primarily rested on the X-ray data and optical data[11] (since the radio data were quite sparse, day 4 and day 17). The limitations naturally propagate to the robustness of their inferences. This caveat notwithstanding, these authors find $f_{eB} \equiv 30$, a factor of $\sim$30 lower than the value we find, suggesting a shock wave velocity of 2.5×10^9 cm s^{-1}. At least within the framework of the SSA+IC model, we believe that our inference is more robust, thanks to our comprehensive radio, millimetre and X-ray data sets.

Another set of comprehensive radio data were presented by Krauss et al. (2012) for days > 20 after the explosion. In their analysis, they assumed equipartition only and found an average velocity of $\approx$25 000 km s^{-1}. Furthermore, assuming $\epsilon_e = 0.1$, they found a mass-loss rate 3.5 times greater than what we find. In view of these differences, we analysed the data presented in Krauss et al. (2012) in the same manner as we analysed the early data set we present above. Our analysis suggests an average shock wave velocity of 18 500 $\pm$ 2000 km s^{-1} at later times (at days > 20). Our derived lower velocity can be explained by a few factors. First, our fitting method allows the electron energy power-law index, p, to vary, while Krauss et al. (2012) keep the power-law index constant. This leads to slightly different values of the peak flux and frequency which in turn leads to a lower value of the velocity. We find an average value of $p = 2.8$, which is the constant value that Krauss et al. use. Another factor that contributes to the difference between Krauss et al. (2012) and our velocity value is the different coefficient used in equation (3). While we are using the coefficient from Chevalier (1998), Krauss et al. (2012) use a coefficient which is larger by 20 per cent. When using Krauss et al. (2012) values for the peak frequencies and fluxes in equation (3) using our coefficient, we find an average shock wave velocity of 21 000 km s^{-1} which is consistent with our results, given our errors.

In light of the above uncertainty in the radius coefficient and in the fitting method (constant versus varying electron power-law index p), we note that the uncertainty in derived values of the shock wave properties is greater than the error measurements alone. The different uncertainties, combined, can be as high as 20–30 per cent. Therefore, any conclusion based on the absolute derived value of the shock wave properties, such as its velocity, is weakened. The time evolution of these properties is less sensitive to the above uncertainties and therefore may provide a more robust diagnostic.

Another method of measuring the shock wave velocity is to directly measure the size of the radio-emitting region using the very long baseline interferometry technique. Such a measurement was performed by Bietenholz et al. (2012) on day 83 after the explosion. Based on their measurement they found that the shock wave velocity is 21 000 $\pm$ 7000 km s^{-1}, which is consistent with both our results and Soderberg et al. (2012) and Krauss et al. (2012) results.

On another matter, thanks to broad banding, improved receivers and a flexible correlator, the EVLA has sensitivity gains ranging from a factor of 2 to 10 in the 1–40 GHz band. Separately, there have been relentless and steady improvements in the continuum sensitivity of millimetre wave arrays (CARMA, PdBI) with the ALMA now offering an order of magnitude increase in sensitivity in the millimetre and submillimetre bands.

These great improvements offer powerful diagnostics in two ways. First, both synchrotron self-absorption and free–free absorption (from the circumstellar medium) depends strongly on frequency. High-frequency observations can be sensibly undertaken at very early times. (EVLA bands are usually self-absorbed at, say, day 1.) Thus, early millimetre wave observations can probe the fastest moving ejecta (since in a homologous flow the fastest moving ejecta are at the greatest radius). Next, the intrinsic SSA spectrum is modified by the external free–free optical absorption. This is best measured by comparing lower frequency measurements to higher frequency measurements. A clear detection of free–free absorption gives a model-independent measure of the density of the CSM.

These two diagnostics motivated our CARMA+EVLA effort. The toy model given in Appendix A shows that a future SN, such as SN 2011dh, if observed at, say, day 1, would allow us to meet at least one of these two goals. Given that surveys such as PTF are now moving to even faster cadence, we would expect these two goals to be realized in the very near future.

ACKNOWLEDGEMENTS

We thank the EVLA and CARMA staff for promptly scheduling this target of opportunity. The National Radio Astronomy Observatory is a facility of the National Science Foundation operated under cooperative agreement by Associated Universities, Inc. Support for CARMA construction was derived from the Gordon and Betty Moore Foundation, the Kenneth T. and Eileen L. Norris Foundation, the James S. McDonnell Foundation, the Associates of the California Institute of Technology, the University of Chicago, the states of California, Illinois and Maryland, and the National Science Foundation. Ongoing CARMA development and operations are supported by the National Science Foundation under a cooperative agreement, and by the CARMA partner universities. This work made use of data supplied by the UK SSDC. PTF is a fully automated, wide-field survey aimed at a systematic exploration of explosions and variable phenomena in optical wavelengths. The participating institutions are Caltech, Columbia University, Weizmann Institute of Science, Lawrence Berkeley Laboratory, Oxford and University of California at Berkeley. The programme is centred on a 12K $\times$ 8K, 7.8 deg^2 CCD array (CFH12K) re-engineered for the 1.2-m Oschin Telescope at the Palomar Observatory by Caltech Optical Observatories. Photometric follow-up is undertaken by the automated Palomar 1.5-m telescope. Research at Caltech is supported by grants from NSF and NASA. The Weizmann PTF partnership is supported in part by the Israeli Science Foundation via grants to AG. The Weizmann–Caltech collaboration is supported by a grant from the BSF to AG and SRK. AG further acknowledges the Lord Sieff of Brimpton Foundation. CS is supported by the NASA Wisconsin Space Grant Consortium. FB acknowledges support from CONICYT, Chile, under grants FONDECYT 1101024 and FONDAPCATA 15010003, Programa de Financiamiento Basal, the Iniciativa

[11] The analysis uses the method of Chevalier & Fransson (2006) which describes the IC emission as a function of optical luminosity, f_{eB}, shock wave velocity, mass-loss rate, wind velocity and time.

Cientifica Milenio through the Millennium Center for Supernova Science grant P10-064-F, and Chandra X-ray Center grants SAO GO9-0086D and GO0-11095A. MMK acknowledges support from the Hubble Fellowship and the Carnegie–Princeton Fellowship. NP acknowledges partial support by STScI-DDRF grant D0001.82435. Research at the Naval Research Laboratory is supported by funding from the Office of Naval Research. SBC acknowledges generous financial assistance from Gary & Cynthia Bengier, the Richard & Rhoda Goldman Fund, the Sylvia & Jim Katzman Foundation, the Christopher R. Redlich Fund, the TABASGO Foundation, and NSF grants AST-0908886 and AST-1211916. We thank the anonymous referee for his constructive comments.

REFERENCES

Arcavi I. et al., 2011a, ApJ, 742, L18
Arcavi I. et al., 2011b, The Astronomer's Telegram, 3413, 1
Arnaud K. A., 1996, in Jacoby G. H., Barnes J., eds, ASP Conf. Ser. Vol. 101, Astronomical Data Analysis Software and Systems V. Astron. Soc. Pac., San Francisco, p. 17
Benvenuto O. G., Bersten M. C., Nomoto K., 2013, ApJ, 762, 74
Bersten M. C. et al., 2012, ApJ, 757, 31
Bietenholz M. F., Brunthaler A., Soderberg A. M., Krauss M., Zauderer B., Bartel N., Chomiuk L., Rupen M. P., 2012, ApJ, 751, 125
Burrows D. N. et al., 2003, in Truemper J. E., Tananbaum H. D., eds, Proc. SPIE Vol. 4851, X-Ray and Gamma-Ray Telescopes and Instruments for Astronomy. SPIE, Bellingham, p. 1320
Chevalier R. A., 1982, ApJ, 259, 302
Chevalier R. A., 1998, ApJ, 499, 810
Chevalier R. A., Fransson C., 2006, ApJ, 651, 381
Chevalier R. A., Soderberg A. M., 2010, ApJ, 711, L40
Evans P. A. et al., 2007, A&A, 469, 379
Fransson C., Björnsson C.-I., 1998, ApJ, 509, 861
Fransson C., Lundqvist P., Chevalier R. A., 1996, ApJ, 461, 993
Katz B., 2012, MNRAS, 420, L6
Krauss M. I. et al., 2012, ApJ, 750, L40
Law N. M. et al., 2009, PASP, 121, 1395
Lundqvist P., Fransson C., 1988, A&A, 192, 221
Maund J. R. et al., 2011, ApJ, 739, L37
Perley R. A., Chandler C. J., Butler B. J., Wrobel J. M., 2011, ApJ, 739, L1
Pooley D., 2011, The Astronomer's Telegram, 3456, 1
Rau A. et al., 2009, PASP, 121, 1334
Readhead A. C. S., 1994, ApJ, 426, 51
Soderberg A. M., Chevalier R. A., Kulkarni S. R., Frail D. A., 2006, ApJ, 651, 1005
Soderberg A. M., Brunthaler A., Nakar E., Chevalier R. A., Bietenholz M. F., 2010, ApJ, 725, 922
Soderberg A. M. et al., 2012, ApJ, 752, 78
Szczygieł D. M., Gerke J. R., Kochanek C. S., Stanek K. Z., 2011, ApJ, 747, 23
Van Dyk S. D. et al., 2011, ApJ, 741, L28
Weiler K. W., Panagia N., Montes M. J., Sramek R. A., 2002, ARA&A, 40, 387
Weiler K. W., Williams C. L., Panagia N., Stockdale C. J., Kelley M. T., Sramek R. A., Van Dyk S. D., Marcaide J. M., 2007, ApJ, 671, 1959

APPENDIX A: WHY EARLY RADIO (CENTIMETRE AND MILLIMETRE) OBSERVATIONS OF SNe ARE IMPORTANT

In this appendix, we discuss the effect of free–free absorption on the observed radio emission when the SN is still very young (one to a few days old). We use the properties of SN 2011dh, found in the above analysis, as an example. While the equations describing free–free absorption were presented many times in the past (e.g. Chevalier 1982; Fransson & Björnsson 1998; Chevalier & Fransson 2006), we repeat some of the equations for the sake of clarity (equations A1– A5).

The free–free optical depth is

$$\tau_{\rm ff} = 3.3 \times 10^{-7} T_4^{-1.35} \nu_{\rm GHz}^{-2.1}\ {\rm EM}, \quad \text{(A1)}$$

where $T = 10^4 T_4$ is the electron temperature (in K),[12] $\nu_{\rm GHz}$ is the frequency in GHz and EM is the emission measure (the integral of $n_{\rm e}^2$ along the line of sight, in units of cm^{-6} pc).

For a star which has been losing matter at a constant rate, $\dot{M}$, the circumstellar density has the following radial profile:

$$\rho(r) = n(r)\mu = \frac{\dot{M}}{4\pi r^2 v_{\rm w}}, \quad \text{(A2)}$$

where $v_{\rm w}$ is the wind velocity, r is the radial distance from the star, n is the particle density and μ is the mean atomic weight of the CSM. Thus, $n(r) \propto r^{-2}$. We assume that the CSM is ionized. This is probably not an issue for blue supergiants or Wolf–Rayet progenitors. The strong UV flash for red supergiants provides some amount of ionization and so a specific check needs to be done for such progenitors. The EM from a radius, say, r_1 to infinity is

$${\rm EM} = \int_{r_1}^{\infty} n_*^2 \left(\frac{r}{r_*}\right)^{-4} {\rm d}r = \frac{1}{3} n_*^2 r_* \left(\frac{r_1}{r_*}\right)^{-3}, \quad \text{(A3)}$$

where n_* is the density of electrons at radius r_*. We choose the following normalization for these two quantities: $n = 10^6 n_6$ and $r = 10^{15} r_{15}$. The corresponding expression for the EM is

$${\rm EM} = 1.08 \times 10^8 n_{*6}^2 r_{*15} \left(\frac{r_{15}}{r_{*15}}\right)^{-3}. \quad \text{(A4)}$$

Using the above equation for the EM and substituting $r_{15} = 0.0864 \times v_9 t_{\rm d}$, the free–free optical depth is

$$\tau_{\rm ff} = 5.5 \times 10^4 n_{*6}^2 r_{*15}^4 v_9^{-3} t_{\rm d}^{-3} T_4^{-1.35} \nu_{\rm GHz}^{-2.1}. \quad \text{(A5)}$$

We use SN 2011dh as an example[13] and set $v_9 = 1.5$, $r_{*15} = 1$ and $n_{*6} = 4.9$. In this case the free–free optical depth is $\tau_{\rm ff} = 6.5 \times 10^2 t_{\rm d}^{-3} T_4^{-1.35} \nu_{\rm GHz}^{-2.1}$. Setting the left-hand side to unity and assuming $T_4 = 100$, based on the early-time temperature of SN 1993J found by Fransson & Björnsson (1998), yields the run of the frequency at which *qualitatively* the optical depth is unity:

$$\nu_{\rm GHz}({\rm ff}) = 23.8 t_{\rm d}^{-1.43}. \quad \text{(A6)}$$

The SSA optical depth is described by

$$\tau_{\rm SSA} = K5 \left(\frac{\nu}{5\,{\rm GHz}}\right)^{\alpha-2.5} \left(\frac{t-t_0}{1\,{\rm d}}\right)^{\delta''}, \quad \text{(A7)}$$

where $K5$ is a proportionality constant that can be determined by fitting the data and δ'' describes the time dependence of the optical depth. In Section 4.2, we found the following parameters for SN 2011dh: $\alpha = -1.15$, $K5 = 1.98 \times 10^5$ and $\delta'' = -3.42$. The SSA optical depth in this case is

$$\tau_{\rm SSA} = 7 \times 10^7 \nu_{\rm GHz}^{-3.65} t_{\rm d}^{-3.42}. \quad \text{(A8)}$$

Setting $\tau_{\rm SSA}$ to unity yields the run of the peak SSA frequency as a function of time:

$$\nu_{\rm GHz}({\rm SSA}) = 141 t_{\rm d}^{-0.937}. \quad \text{(A9)}$$

[12] We use the convention of $X_n = X/10^n$ where it is assumed, unless explicitly specified, that the units are in cgs.
[13] Here we use the lower velocity and the higher electron density that we found for the non-equipartition case.

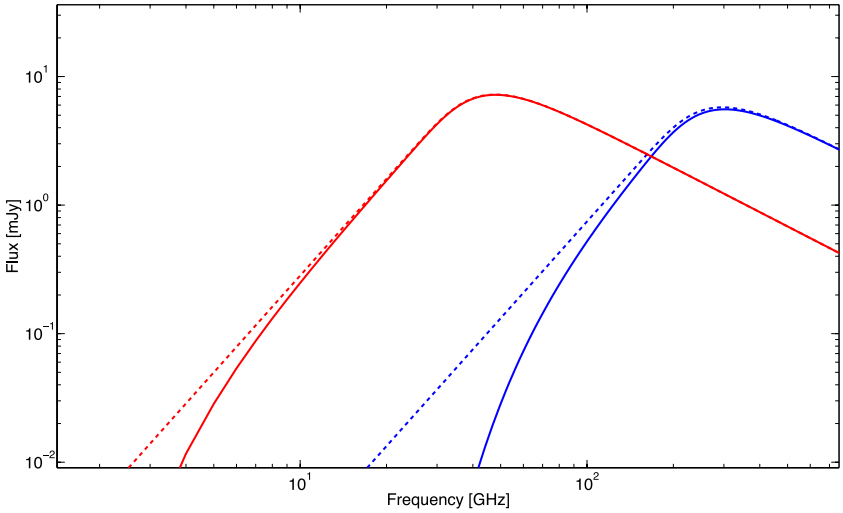

Figure A1. Theoretical radio spectra of SNe, including synchrotron-self absorption and with (solid lines) or without (dashed lines) free–free absorption. The blue and red lines are for days 1 and 4 after explosion, respectively. The above spectra were produced using equations (5), (A5) and (A8) with the fitted parameters found in Section 4.2 for SN 2011dh.

Armed with equations (A5) and (A8) with the fitted parameters we found in Section 4.2, we can now look into the value of even earlier mm observations (see Fig. A1). Had we observed SN 2011dh on day 1, the EVLA observations could have shown signatures of free–free absorption. We also note that $\tau_{\rm ff}$ is proportional to $n_*^2 r_*$, whereas the SSA optical depth is a different function of n_* and r_*. Thus, we can, in principle, obtain a different measure of n_* and r_*.

This paper has been typeset from a TEX/LATEX file prepared by the author.